

Quantum communication networks with defects in silicon carbide

Philipp Sohr,^{1,2,3,*} Philipp Koller,^{1,4} Sebastian Ecker,³ Matthias Fink,³ Thomas Scheidl,³ Rupert Ursin,³ Muhammad Junaid Arshad,⁵ Cristian Bonato,⁵ Pasquale Cilibrizzi,⁵ Adam Gali,^{6,7,8} Péter Udvarhelyi,^{6,7} Alberto Politi,⁹ Oliver J. Trojak,⁹ Misagh Ghezellou,¹⁰ Jawad Ul Hassan,¹⁰ Ivan G. Ivanov,¹⁰ Nguyen Tien Son,¹⁰ Guido Burkard,¹¹ Benedikt Tissot,¹¹ Joop Hendriks,¹² Carmem M. Gilardoni,¹² Caspar H. van der Wal,¹² Christian David,¹³ Masa Mokhtarzadeh,¹³ Thomas Astner,¹ and Michael Trupke^{1,†}

¹*Institute for Quantum Optics and Quantum Information (IQOQI),
Austrian Academy of Sciences, Boltzmannngasse 3, 1090 Vienna, Austria*

²*Vienna Center for Quantum Science and Technology, Atominstitut, TU Wien, 1020 Vienna, Austria*

³*Quantum Technology Laboratories GmbH (qtlabs),
Clemens-Holzmeister-Straße 6/6, 1100 Vienna, Austria*

⁴*University of Vienna, Faculty of Physics & Vienna Doctoral School in Physics, Boltzmannngasse 5, A-1090 Vienna, Austria*

⁵*Institute of Photonics and Quantum Sciences, SUPA,
Heriot-Watt University, Edinburgh EH14 4AS, United Kingdom*

⁶*HUN-REN Wigner Research Centre for Physics, PO. Box 49, H-1525 Budapest, Hungary*

⁷*Department of Atomic Physics, Institute of Physics,
Budapest University of Technology and Economics,
Műegyetem rakpart 3., H-1111 Budapest, Hungary*

⁸*MTA-WFK Lendület "Momentum" Semiconductor Nanostructures Research Group, PO. Box 49, H-1525 Budapest, Hungary*

⁹*School of Physics and Astronomy, University of Southampton, Southampton SO17 1BJ, United Kingdom*

¹⁰*University, Department of Physics, Chemistry and Biology, SE-58183 Linköping, Sweden*

¹¹*Department of Physics, University of Konstanz, D-78457 Konstanz, Germany*

¹²*Zernike Institute for Advanced Materials, University of Groningen, NL-9747AG Groningen, The Netherlands*

¹³*Paul Scherrer Institut, CH-5232 Villigen, Switzerland*

Quantum communication promises unprecedented capabilities enabled by the transmission of quantum states of light. However, current implementations face severe distance limitations due to photon loss. Silicon carbide (SiC) defects have emerged as a promising quantum device platform, offering strong optical transitions, long spin coherence lifetimes and the opportunity for integration with semiconductor devices. Some defects with optical transitions in the telecom range have been identified, allowing to interface with fiber networks without the need for wavelength conversion. These unique properties make SiC an attractive platform for the implementation of quantum nodes for quantum communication networks. We provide an overview of the most prominent defects in SiC and their implementation in spin-photon interfaces. Furthermore, we model an exemplary, memory-enhanced quantum communication protocol in order to extract the parameters required to surpass a direct point-to-point link performance. Based on these insights, we summarize the key steps required towards the deployment of SiC devices in large-scale quantum communication networks.

I. Introduction

The advent of the information age is driven not by computers alone, but increasingly by the connections between many computers into ever-growing information processing networks. Similarly, quantum links will prove essential in distributed quantum computing and quantum sensing [1, 2]. A key step on this path is the exploitation of quantum properties for the communication process itself.

The exchange of photons in quantum communication enables communication primitives that are unachievable in the classical realm. In quantum cryptography, for example, quantum states of light are used to exchange cryptographic keys which are inaccessible by a third party by

virtue of the no-cloning theorem [3, 4]. The main roadblock towards widespread deployment of quantum cryptography is the limited communication distance of a few 100 km in optical fiber due to the absence of a quantum amplifier. Currently, there are two approaches of extending the transmission distance of flying qubits. The first one involves free-space links between optical ground receivers and satellites, an approach which has seen the first in-field demonstrations in recent years [5]. Satellite-based quantum communication enables exchange of cryptographic keys around the globe [6, 7], where the loss is dominated by diffraction instead of absorption. The second approach relies on intermediate nodes in fiber-based networks, which promise to overcome the fundamental limit of point-to-point connections [8]. These nodes interface flying qubits with stationary qubits. Not only do stationary qubits act as quantum memories to extend the transmission distance of quantum states, but they also facilitate processing and routing of quantum information in complex network topologies.

* philipp.sohr@student.tuwien.ac.at

† michael.trupke@oeaw.ac.at

Quantum nodes should therefore simultaneously fulfill several requirements. First and foremost, the transfer of quantum information to and from the nodes should be faithful and efficient [9]. Secondly, the storage time, which is limited by decoherence effects of the underlying physical system is crucial. In particular, it should be long enough to enable local quantum processing in addition to quantum and classical communication, both of which are limited by the travel time of the photons over global distances and the success probability of photon transmission. Ideally, the state can be transferred from the spin memory to a long-lived quantum register with a storage time which is longer by orders of magnitude [10]. Crucially, the memories should operate at one of the telecommunication wavelength bands in order to minimize transmission losses and guarantee compatibility with existing fiber infrastructure. While quantum frequency conversion is a viable solution for shifting frequencies to the telecommunication band [11–13], added noise and losses are inevitable. In addition, the nodes should be hosted on a scalable and integrated platform for parallelization and multiplexing purposes.

While several candidate systems, such as atomic ensembles [14], quantum dots [15, 16], rare-earth-doped solids [17, 18] and trapped ions [19] are currently being investigated, defects in semiconductor materials are a particularly promising platform: They offer a view to scalable fabrication, integration with electronics, and compatibility with the highly advanced tools and methods of the semiconductor industry. Among these, a number of defects in silicon carbide have gained attention due to their strong optical transitions and long spin coherence lifetimes [10, 20, 21].

A central concept in the deployment of semiconductor defects for quantum networks is spin-photon entanglement. Spin centers can be interfaced with photonic time-bin qubits as well as polarization qubits, making them versatile and deployable for both free-space and fiber-optical quantum communication [22–25]. These hybrid entangled states between a stationary and a flying qubit facilitate heralded entanglement between two quantum memories via Bell state measurements (BSM). To this end, two photons are interfered on a beamsplitter in a synchronous BSM, or a single defect is read out after two consecutive writing processes, which constitutes an asynchronous BSM [26, 27]. BSMs are also key in entanglement swapping, which in turn is an essential building block of the quantum repeater protocol [8]. While impressive progress has been achieved, including demonstrations of heralded entanglement distribution between quantum memories and basic quantum network operations [17, 18, 28–31], fully-fledged quantum repeater chains which outperform point-to-point connections in quantum cryptography remain an outstanding challenge. However, several quantum cryptography protocols exhibit a substantial benefit over the direct transmission of photons with only a single intermediate network node. One of these protocols is memory-assisted quantum key

distribution (MA-QKD) [26], which is regarded as an important milestone on the path to outperforming direct transmission [32].

In this work, we present the results of MA-QKD simulations with parameters from state-of-the-art SiC devices. This approach serves as a testbed for the performance of SiC memories in a relevant quantum communication setting. The results of this study provide the basis for the development of a roadmap for SiC devices. Furthermore, we discuss advanced quantum communication scenarios which benefit from the SiC platform. This paper is organized as follows. In Sec. II A we introduce the silicon carbide platform and some of the defects which are of interest, while Sec. II B is devoted to the photonic properties of the defects and their integration in quantum devices. We describe how these quantum devices based on SiC are suited as quantum nodes in Sec. III A. After a short introduction to quantum cryptography, Sec. III B is dedicated to a particular memory-assisted QKD protocol, with secure key rate simulation results presented in Sec. III C. We draw a roadmap for necessary improvements of SiC devices for quantum link deployment in Sec. IV and conclude with a summary in Sec. V.

II. The silicon carbide platform

A. Implementing spin-photon interfaces with defects in SiC

Single electron spins may be optically accessed through point defects in semiconductors, such as SiC [33]. The electron spin of the isolated paramagnetic defects in SiC can serve as a solid-state qubit once it can be initialized, read out and coherently controlled [22, 34–39]. Furthermore, nuclear spins of the host crystal proximate to the point defects, e.g., ^{13}C and ^{29}Si in SiC, or introduced by the defect itself, e.g., ^{14}N or ^{15}N in nitrogen-vacancy defects [37, 40–47] or ^{51}V in substitutional vanadium defects [48–50], can be used as quantum registers or ancilla qubits mediated by the hyperfine interaction between them (e.g., Refs. 51–53). The quantum states of the electron spin and nuclear spins can be typically controlled by microwave and radio-frequency alternating magnetic fields, if necessary, in the presence of a constant magnetic field.

A coherent spin-photon interface (SPI) can be created by exploiting spin-dependent atomic-like optical transitions [22, 39, 54, 55], typically available at cryogenic temperature. Spin-selective optical transitions, possibly in combination with microwaves for higher-spin systems, enable the preparation of specific spin states by optical pumping [55, 56]. They also enable readout by detection of the emitted photons under optical excitation [54], or by conversion of spin-states into different charge states [57–59]. Coherent SPIs also enable to establish a connection between the quantum memory of the solid-state qubit and the flying qubit encoded into the chosen quantum

property of the photon [22]. This can be harnessed to setup entanglement-based quantum communication. Recently, the first demonstration of spin-photon entanglement with a SiC defect was reported using the silicon vacancy in 4H-SiC [60].

Architectures based on single point defects in materials with a diluted nuclear spin bath have also shown the promising opportunity to coherently control a register of nearby weakly-coupled nuclear spins [61]. In this case, the hyperfine interaction acts on timescales longer than the electron spin dephasing time, so that it does not result in a separate transition visible in the electron spin resonance spectrum and cannot be driven directly. Nonetheless, it is possible to address and coherently control such nuclear spins by applying pulse sequences such as dynamical decoupling on the electron spin, that extend its coherence time and can effectively isolate the contribution of a single, weakly-coupled nuclear spin, filtering out all the other background. These techniques have enabled the implementation of multi-qubit schemes [62], such as quantum error correction [63]. While most of this work has been done in diamond, some recent results show that it is also possible in SiC [53]. Given the higher abundance of isotopes with non-zero nuclear spin in SiC, however, isotopic engineering may be required to maximize the number of controllable nuclear spins [64].

We note that the reduction of the density of ^{13}C and ^{29}Si nuclear spins can be advantageous to extend the coherence times and reduce the optical linewidth of the coherent emission [39, 53], which occurs at the zero-phonon-line (ZPL) emission of the defects. It is imperative to fully characterize the magneto-optical properties of these point defects, in order to develop efficient quantum optics protocols for quantum information processing applications such as quantum communication.

The most mature polytype of SiC is 4H-SiC which has a band gap of 3.3 eV. To realize a spin-to-photon interface, deep levels should be introduced by the point defect. This can typically be achieved by introducing dangling bonds of vacancies or dopants with d and f orbitals. We illustrate this by comparing three types of deep-level point defects in SiC: the silicon-vacancy (Si-vacancy), divacancy and vanadium centres in 4H-SiC (see Fig. 1). These defects introduce multiple levels into the band gap where the excited state can be described by promoting an electron from the occupied in-gap level to the unfilled in-gap level. These defects have complementary ground state spin structure, with the the negatively charged Si-vacancy having spin $S = 3/2$ in an orbital singlet, the neutral divacancy spin $S = 1$, and the neutral vanadium substituting silicon has spin $S = 1/2$ in an orbital doublet.

The electron-orbital and spin level structures are depicted for the three selected qubit species (see Fig. 1). For the negatively charged Si-vacancy in 4H-SiC, in-gap localized defect states are generated by the four carbon dangling bonds of the defect which lead to non-degenerate and triple-degenerate orbitals occupied by five

electrons. The latter splits due to the C_{3v} symmetric crystal field of the defective 4H-SiC lattice. Finally, these defect states constitute an orbital singlet $^4A_2(g)$ ground state and an orbital triplet $^4T_2(e)$ excited state, where the latter splits to $^4A_2(e)$ and $^4E(e)$ states in ascending order for the reason given above [65]. We note that the strength of the crystal field and the energy spacing between these levels depends on the actual defect site and in 4H-SiC the splitting is larger for the Si-vacancy defect at the quasicubic site [66]. We continue with that Si-vacancy configuration in 4H-SiC. At low temperatures, the fluorescence is dominated by the $^4A_2(e) \rightarrow ^4A_2(g)$ optical transition which results in the so-called V2 PL spectrum with zero-phonon-line (ZPL) wavelength at 917 nm (1.35 eV) (see Ref. 65 and references therein). The $m_S = \pm 1/2$ and $m_S = \pm 3/2$ states of the quartet spin slightly split by the so-called zero-field-splitting of about 70 MHz due to the crystal field. With optical excitation of this system, the electron spin can be pumped into the $m_S = \pm 1/2$ in the electronic ground state, and the photoluminescence is brighter for the $m_S = \pm 1/2$ states than that for $m_S = \pm 3/2$ states. The origin of the spin-selective fluorescence comes from the spin-selective intersystem crossing between the $^4A_2(e)$ state and the series of spin doublet excited states lying between the quartet states [67–75], see also Fig. 1(b). At zero external magnetic field, radiofrequency magnetic fields can rotate the electron spin in the ground state manifold. This electron spin resonance frequency can be increased to the microwave regime upon applying an appropriate external magnetic field aligned with the c -axis (defect symmetry axis or crystal stacking axis, see Fig. 1(a)) of 4H-SiC.

The neutral divacancy [34, 76–80] in SiC consists of neighbouring Si and C vacancies in the SiC lattice [see Fig. 1(c)]. The electronic structure is identical to the NV centre in diamond, with C_{3v} symmetry and a $S = 1$ electronic spin, so that spin-conserving cyclic transition between $^3A_2 \rightarrow ^3E$ can be used for spin-photon interfacing [22]. Difference from the NV centre are the emission wavelength in the near-infrared (with zero-phonon lines around 1030-1130nm) and a zero-field splitting of about 1.3 GHz. Experimental progress on the divacancy has been quite fast with several breakthroughs, such as long spin coherence time, single-shot electron spin readout [59] and control of associated nuclear spins [53] demonstrated in just a few years.

Another configuration of interest is an electron with $S = 1/2$ within a doublet orbital state. This provides altogether 2×2 quantum states that split into two doubly degenerate Kramers states due to spin-orbit coupling. The Kramers degeneracy can be further split by magnetic fields. Neutral vanadium substituting the silicon in the SiC forms such a system. The in-gap defect states come from the vanadium d orbitals, which are five-fold degenerate under spherical symmetry. The crystal field provided by the SiC lattice splits these d orbitals into a low-energy orbital doublet – which interacts weakly with the lattice – and an orbital triplet higher in energy that hybridizes

tonic crystals or optical waveguides and open microcavities [105–107]. These parameters and properties make the α vanadium center in 4H-SiC very promising candidate to realize a practical SPI with a programmable nuclear spin quantum memory.

We note that the single vanadium centers have been created in SiC by vanadium ion implantation, followed by high-temperature annealing to repair lattice damage of the crystal lattice [38, 39]. The residual parasitic defects after annealing may create strain and fluctuating charge environment upon illumination. This is an important issue in securing stable emission from single vanadium centers and producing indistinguishable quantum emitters for quantum communication. Vanadium in isotopically purified 4H-SiC has a remarkably narrow distribution of central emission frequencies. However, the linewidth of the emission remains several orders of magnitude larger than the Fourier limit [39]. This broadening is believed to be caused by charge fluctuations in the vicinity of the defect under illumination. The fluctuating charges may be depleted by integrating the vanadium centers into p-i-n junctions of 4H-SiC and applying an appropriate electric field, a method which is already established for isolated divacancy qubits [108]. A recent study on single vanadium centers in 4H-SiC has shown that the photostability of single α centers upon illumination can be significantly improved by compensating the residual n-type and p-type dopants of SiC and pinning the Fermi-level to the middle of the band gap [39]. Further spin centres in SiC have recently been studied which possess bright ZPL emission in the telecom domain, including vanadium in 3C-SiC at 1495 nm and the family of chlorine-related defects, with ZPL wavelengths between 1330 nm and 1590 nm [109, 110], and much remains to be discovered regarding the properties of these and other, as yet unknown, spin centres in SiC.

B. SiC photonics

SiC is a mature platform for microelectronics, in particular for power applications. Capitalizing on a wider bandgap, higher thermal conductivity, and larger critical electric field than silicon, SiC devices can operate at higher temperatures, higher current density, and higher blocking voltage and are becoming more and more widespread in applications such as power conversion in electric vehicles [111, 112]

Recently, researchers have begun to explore SiC applications beyond power devices [113, 114]. While it is not a material widely utilised in photonics applications yet, it exhibits rather promising optical properties [20]. Due to its wide bandgap, SiC presents a wide transparency window, between 0.37 - 5.6 μm for the 4H polytype [115–117].

SiC also features fairly strong nonlinear coefficients, not far from values reported for silicon and lithium niobate. The quadratic nonlinearity $\chi^{(2)}$ has been measured

to be ≈ 12.5 pm/V in the hexagonal polytypes [118], while the third order (Kerr) nonlinearity $\chi^{(3)}$ is about $6.9 \times 10^{-19} \text{m}^2/\text{W}$ at 1550 nm [119] for 4H-SiC. Strong nonlinear coefficients are crucial to implement on-chip modulators and frequency converters [120–123].

Given its outstanding electronic and photonic properties, SiC provides a formidable platform for integration of different functionalities into the same chip. It is possible to envision a single quantum photonic chip integrating SPI's with all photonic elements required to process quantum states of light (such as optical modulators or beamsplitters), all electrically controlled.

One crucial step for high-rate spin-photon interfacing is to enhance light-matter interaction with an optical cavity. Enhancement of light-matter interactions using cavity quantum electrodynamics (CQED) can broadly be divided into two approaches: on the one hand, cavities can increase the photon emission from defects into a desired spatial mode, on the other hand a cavity can enhance interaction of an incoming light pulse with the optical dipole. We will briefly describe both approaches below.

The enhancement factor for the spontaneous emission into the cavity, F_{SE} is given by

$$F_{SE} = \frac{3}{4\pi^2} \Upsilon \frac{\gamma_{ZPL}}{\gamma_{tot}} \zeta^2, \text{ with } \Upsilon = \left(\frac{\lambda}{n}\right)^3 \frac{Q}{V}, \quad (1)$$

with the free-space wavelength λ , the refractive index of the material n , the quality factor Q , and the mode volume V . We have furthermore defined the optical enhancement factor Υ which collects the performance parameters of the cavity. The value $\zeta \in [0, 1]$ gives the overlap of the defect's dipole with the electric field mode, relating both to the relative orientation of the dipole and its position within the spatial distribution of the mode, while γ_{ZPL} and γ_{tot} are the decay rate into the zero-phonon line and the total decay rate, respectively [124, 125].

Further, an incoming light pulse will interact more strongly with the optical dipole transition of the defect if it is placed in a suitable cavity. If transitions of different spin states can be resolved, the latter mechanism can be implemented for spin-dependent absorption, reflection, or phase shifting of the incoming light. For a symmetric, lossless cavity, the fractions of the resonant optical power reflected and transmitted by the coupled system are given by [126]

$$R_C = \left(\frac{2C}{2C+1}\right)^2 \text{ and } T_C = \left(\frac{1}{2C+1}\right)^2, \quad (2)$$

where $C = F_{SE}/2$ is the cooperativity of the system. For finite cooperativity, a fraction of the light will be scattered and lost by the system and is given by $S_C = 4C/(2C+1)^2$. Such scattering processes can further lead to undesired spin flips. These expressions assume low-power excitation, i.e. far below the saturation power of the system.

The last few years have seen strong progress in the development of SiC microcavities [10, 20]. An important starting point is the fabrication of thin SiC membranes. Few-microns thick membranes on a high-reflectivity Distributed Bragg Reflector (DBR) can be used for open microcavities, positioning a second concave DBR on top of the emitter [127]. Thinner suspended membranes (few hundred nanometers thick) are required to fabricate photonic crystal devices such as photonic crystal nanocavities and nanobeams. Seminal papers have demonstrated the fabrication of membranes and cavities [105, 128–130] by electro-chemical etching, exploiting the etching selectivity between regions of different doping. More recently, researchers have developed thin-film SiC on insulator, by bonding SiC on a SiO₂-on-Si wafer, and grinding/polishing the SiC to the desired thickness [10]. This technique can deliver wafer-scale thin-film SiC with low roughness, and has been used to fabricate different types of microcavities [131, 132]. However, such processes are currently hampered by non-uniformity of the SiC thickness, leading to low yield in photonic device fabrication.

SiC photonic crystal cavities have reached extremely high quality factors of 6.3×10^5 while maintaining a small mode volume of $2.1 (\lambda/n)^3$, corresponding to $\Upsilon = 3 \times 10^5$ [133]. While integration of SiC with Fabry-Pérot resonators at telecom wavelengths remains unreported, recent work has demonstrated SiC membrane-based microcavities at a different wavelength regime [134], indicating promising potential for future development. In the telecom domain, a Fabry-Pérot microcavity containing an yttrium orthosilicate (YSO) membrane reached $\Upsilon = 7 \times 10^3$ [135]. Recently, microcavities with smaller mode volume and higher finesse have been demonstrated, indicating that $\Upsilon = 2 \times 10^4$ could be reached for SiC [127]. While the enhancement factor is expected to be lower than for optimized photonic crystal cavities, Fabry-Pérot microcavities offer highly efficient coupling to single-mode fibers and integration with micro-electro-mechanical systems for individual tuning in large-scale systems [136].

From a combination of measurements and *ab-initio* calculations, vanadium on the α site of 4H SiC is expected to have a branching ratio of $\gamma_{ZPL}/\gamma_{tot} \simeq 9\%$ [81], giving C approaching 100 for the best reported Fabry-Pérot microcavities, and even approaching 1000 for the best reported photonic crystal cavities, respectively [127, 133]. In both cases, high contrast between coupled and uncoupled spin states can be expected.

III. Beyond point-to-point quantum key distribution with SiC devices

In the following, we focus on applying SiC devices in quantum key distribution (QKD), which is arguably the most mature family of quantum communication protocols. This approach is particularly useful, since the performance of SiC devices in quantum networks can now

be assessed and optimized based on a single parameter, namely the secure key rate (SKR) in QKD, which is the rate of distributed bits that can be used for encryption purposes. The SKR can be used as a key performance metric for quantum networks, as it depends not only on the achievable photon throughput but also on errors arising during transmission and imperfections inherent to the devices. In direct transmission, the SKR is limited by the photon repetition rate of the source and the time resolution of the detection system. In memory-enhanced quantum networks, processing time, communication latency, and quantum node efficiency additionally limit the SKR, along with system noise, as will be discussed in this chapter.

In QKD, two parties, Alice and Bob, aim to establish a secret key with information-theoretic security. Alice encodes raw key in qubits prepared in randomly chosen conjugate bases, while Bob measures them using bases randomly selected from the same set. They retain the secure key bit from events where their basis choices match. Due to the no-cloning theorem [3, 4], a third party is fundamentally incapable to obtain the key without prior knowledge of Alice's or Bob's basis settings. Any eavesdropping attempt disturbs the quantum state, revealing an adversary. There are two families of QKD protocols. In the prepare-and-measure type (e.g. the BB84 protocol [137]), Alice prepares the quantum states and sends them to Bob, who performs measurements. Entanglement-based protocols (e.g. the BBM92 protocol [138]) consist of a central node which distributes pairs of entangled photons to Alice and Bob, both of which perform measurements on their received photon.

Practical implementations of QKD over long distances are mainly impeded by photon loss in optical fibers. The loss of photons leads to an exponential decrease of the SKR with fiber distance, limiting the maximal key exchange distance to a few hundred kilometers in optical fiber [139]. This is the case for a direct fiber connection between Alice and Bob. An alternative approach is the division of the total distance between Alice and Bob into several segments. The loss in each of these segments is reduced exponentially, leading to a substantial improvement in the SKR between Alice and Bob. There are two fundamentally different approaches which make use of this segmentation. The first approach is known as a trusted repeater, where each of the nodes connecting two segments performs a full QKD protocol and the resulting key is relayed to other segments. While this indeed increases the possible transmission distance indefinitely, each node reads out the key, which necessitates absolute trust in each node. The second approach is known as a quantum repeater [8, 140]. Here, adjacent nodes are supplied with entangled photons which are stored in quantum memories. Once the quantum memories of all nodes are loaded, nested entanglement swapping is performed in order to entangle the end nodes which belong to Alice and Bob. With entanglement at hand, Alice and Bob can now perform any quantum communication protocol

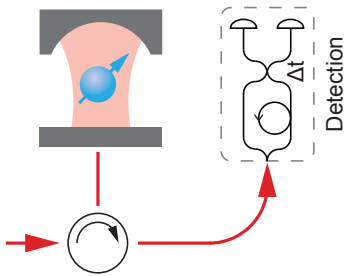


FIG. 2. Configuration of a CQED device enabling a heralded quantum memory and an asynchronous Bell state measurement (BSM). The time-bin state of an incoming photon is converted into spin-photon entanglement between the electron spin and an outgoing time-bin encoded photon. A measurement of the reflected photon in an imbalanced Mach-Zehnder interferometer with imbalance Δt transfers the state of the initial photon onto the spin state, heralded by a single-photon detection event.

using entanglement as a resource [141].

SiC devices are natural candidates for this purpose, since quantum repeater stations must facilitate the storage of qubits over long periods of time and process stored qubits for entanglement distillation [142]. Despite their potential, current SiC devices, as well as other quantum memory platforms, are unable to fulfill the stringent requirements of quantum repeaters, let alone the necessary error correction or entanglement distillation overheads, and therefore fail to outperform direct transmission of photons. However, there are QKD protocols which exhibit a quantum memory enhancement without requiring a fully-fledged quantum repeater chain [32, 143].

We focus on one particular protocol, so-called memory-assisted measurement-device-independent QKD (MA-MDI-QKD) [26], which requires only a single quantum repeater node. First, we cover the deployment of SiC devices as quantum nodes and discuss to what extent they fulfill the requirements for quantum communication. We then go through the MA-MDI-QKD protocol in greater detail and simulate the protocol based on realistic parameters of state-of-the-art SiC devices. Additionally, we discuss the opportunities of SiC devices for advanced quantum network architectures.

A. SiC devices as quantum nodes

SiC devices serve as an SPI, enabling the transfer of a photon's quantum state to an electronic spin state and vice versa. A device configuration implementing this interface is sketched in Fig. 2 and discussed below. After the qubit is stored in the spin state, we can apply arbitrary unitary operations using microwave pulses. To connect two quantum links, we need to perform at least two-qubit gates in the quantum node.

The SPI primarily relies on spin-photon entanglement.

Let us consider the writing process of a photonic qubit state into the quantum memory. We use time-bin encoding of the photon, although it is worth noting that SiC memories can also be connected to other degrees of freedom, such as polarization. A time-bin qubit

$$|\Psi\rangle_{\text{photon}} = \frac{1}{\sqrt{2}} (|t_1\rangle + e^{i\phi} |t_2\rangle), \quad (3)$$

is realized as a coherent superposition of two orthogonal states, corresponding to the presence of a photon at time t_1 and at a later time t_2 . The electron spin is initialized in state

$$|\Psi\rangle_{\text{spin}}^{\text{init}} = \frac{1}{\sqrt{2}} (|\downarrow\rangle + |\uparrow\rangle), \quad (4)$$

where $|\downarrow\rangle$ ($|\uparrow\rangle$) corresponds to the spin down (up) state of the electron. Based on the non-degenerate level structure [144], a photon arriving at time t_1 is resonant only with the optical transition of state $|\downarrow\rangle$ and is thus reflected off the defect-cavity system via coherent scattering, resulting in the joint spin-photon state $|\downarrow t_1\rangle$. Between t_1 and t_2 , a π -pulse is applied to the microwave transition, which inverts the electron spin state swapping $|\downarrow\rangle$ and $|\uparrow\rangle$. The later time-bin $|t_2\rangle$ is again resonant with the optical transition of state $|\downarrow\rangle$, and upon successful reflection and another π -pulse results in state $|\uparrow t_2\rangle$. Both the population transfer between the electronic spin states and the time-bin state are coherent processes, resulting in a coherent superposition of spin-photon states.

$$|\Psi\rangle_{\text{spin-photon}} = \frac{1}{\sqrt{2}} (|\downarrow t_1\rangle + e^{i\phi} |\uparrow t_2\rangle), \quad (5)$$

describing a spin-photon-entangled state.

An optical circulator directs the reflected photon to a detection unit, comprising a Mach-Zehnder interferometer with imbalance $\Delta t = t_2 - t_1$ and single-photon detectors (see Fig. 2). The interferometer implements a probabilistic measurement in the X-basis $\{(|t_1\rangle + |t_2\rangle)/\sqrt{2}, (|t_1\rangle - |t_2\rangle)/\sqrt{2}\}$. Detection of the photon in this basis transfers the initial photonic qubit state onto the spin state, resulting in

$$|\Psi\rangle_{\text{spin}}^{\text{final}} = \frac{1}{\sqrt{2}} (|\downarrow\rangle + e^{i\phi} |\uparrow\rangle), \quad (6)$$

where the measurement-induced phase ambiguity, resulting from the probabilistic registration in one of the two single-photon detectors after the Mach-Zehnder interferometer, has already been compensated [145].

The detection of a single photon after the interferometer heralds the successful writing process of the initial photon state to the spin state memory. The overall efficiency of the described writing process is limited to a maximum of 25%, stemming from two probabilistic steps: the state-dependent photon reflection at the cavity succeeds only in 50% of the cases, and the projective measurement in the Mach-Zehnder interferometer also

succeeds only in 50 % of the cases [146]. This photon loss after interaction with the spin-cavity system not only reduces the SKR due decreased signal intensity but also introduces noise at the memory loading stage [147].

Two-qubit gates play a crucial role in quantum communication, especially for achieving a BSM between two incoming photons. SiC devices provide a suitable approach to perform this BSM asynchronously using a single defect [27]. After writing the first photon in the spin memory, a second photon with phase ϕ' can be loaded into the same defect memory. The resulting spin state

$$|\Psi\rangle_{\text{spin}}^{\text{BSM}} = \frac{1}{\sqrt{2}} \left(|\downarrow\rangle + e^{i(\phi+\phi')} |\uparrow\rangle \right), \quad (7)$$

inherits the sum of the phases of both photons. Once more, the phase ambiguity that arises after photon measurement has already been compensated for. The BSM is concluded by reading out the spin state in the X-basis. Depending on the measurement outcome, two Bell states, namely the Φ^+ or the Φ^- state, can be discriminated. While the asynchronous BSM is resource efficient – only a single quantum memory is required – both photons enter the cavity via the same single-mode fiber. To prevent additional channel losses caused by probabilistic routing with a beamsplitter [27], active optical switching can be implemented instead.

B. Memory-assisted measurement-device-independent QKD

Measurement-device-independent (MDI) QKD can be viewed as an entanglement-based QKD protocol in reverse. In entanglement-based QKD a central source produces pairs of entangled photons and transmits them to the communicating parties Alice and Bob. In MDI QKD, both Alice and Bob randomly and independently prepare photons in one of the four BB84 states $\{|0\rangle, |1\rangle, (|0\rangle \pm |1\rangle)/\sqrt{2}\}$ [137] and send them to a third, untrusted party, called Charlie (C) (see Fig. 3). Charlie performs a BSM, projecting the separable state of Alice’s and Bob’s photon on a joint state in the Bell basis. Following Charlie’s announcement of the BSM outcome, Alice and Bob publicly disclose their basis choices, retaining only instances where their bases match and discarding the rest. Based on Charlie’s announcement, Alice or Bob adjust their bit values as necessary to ensure correlation of their bit strings.

This protocol is measurement-device-independent, since it avoids known side-channel attacks and vulnerabilities of the detectors [148]. The protocol requires that both Alice’s and Bob’s photon arrive simultaneously at the BSM. With increasing channel loss, the probability of two photons arriving simultaneously decreases exponentially.

The efficiency of this protocol can be significantly bolstered by temporarily storing qubits at the central node prior to the BSM. Such storage enables synchronisation

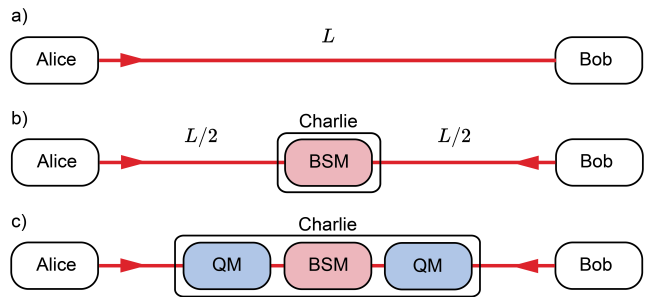


FIG. 3. Comparison between different QKD schemes. a) In prepare-and-measure-type QKD protocols (e.g., BB84), Alice produces quantum states and sends them to Bob over a channel of length L . Bob performs measurements. b) In measurement-device-independent (MDI)-QKD protocols, Alice and Bob each prepare quantum states and send them to Charlie, an untrusted third party located at the channel midpoint (channel segment length $L/2$). Charlie performs a Bell state measurement (BSM) on both quantum states and based on the outcome of this measurement, Alice and Bob agree on a secret key. c) In memory-assisted measurement-device-independent (MA-MDI)-QKD, both Alice and Bob produce quantum states and send them to Charlie. Prior to the BSM, Charlie synchronises the arrival of the quantum states with the help of quantum memories (QM). Upon successful BSM, Charlie announces the outcome of the measurement which leads to the establishment of a secret key between Alice and Bob.

of Alice’s and Bob’s channels [26], eliminating the need for precise simultaneous photon arrival. The BSM is then executed asynchronously, exclusively upon the complete loading of both memories. In essence, this scheme merges ideas from quantum repeaters and MDI-QKD and is among the simplest QKD protocols involving quantum memories. We discuss this protocol as it provides a straightforward performance comparison to direct photonic QKD systems. More advanced methods may allow to further increase the quantum communication rates using scalable spin-photon interfaces [149–151].

The asynchronous BSM introduced in the previous section is perfectly suited for MA-MDI-QKD with minor modifications. Alice and Bob each randomly and independently choose their basis as well as their bit value. They prepare time-bin states, such as described in Equation (3) and encode their bit choice in the relative phases $\{0, \pi\}$ and $\{\pi/2, -\pi/2\}$ for the X and the Y basis respectively. The qubits follow one after another with the same temporal spacing as the two time-bins forming a qubit. Neither do qubits interleave, that is, share the same time-bin, nor is there extra spacing between successive qubits. Since both Alice’s and Bob’s photons must be guided to the same SPI and the sender of each photon must be unambiguously identified, optical switching is required. An efficient solution to this problem is to use two SiC devices and an optical switch which re-routes the fibers after the first detection event (see Fig. 4). This toggling prevents the node C from being idle and is a first step

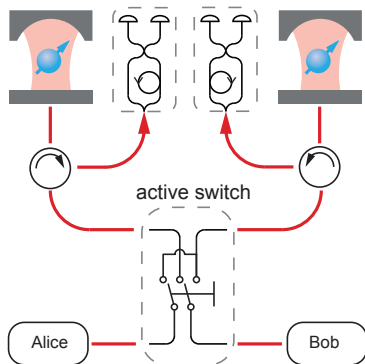


FIG. 4. Two CQED devices receiving photons from Alice and Bob via an optical switch. Each of the devices can perform asynchronous Bell state measurements. In order to avoid idle time of the central node, the optical switch toggles Alice’s and Bob’s fibers after successful detection of one photon either from Alice or Bob.

towards parallelization (see Sec. IV). This is one crucial technological step beyond the first demonstration of a memory-assisted QKD protocol in Ref. [27], where the authors employ a probabilistic routing of the photons. In detail, the following switching rules are applied for this work:

1. Initialize memory in state $|\Psi\rangle_{\text{spin}}^{\text{init}}$, see Equation (4).
2. Switch as soon as the successful loading of at least one memory is heralded.
3. Perform BSM readout as soon as the successful loading of at least one memory, loaded already in step 2, is heralded.
4. In case of successful BSM or maximal waiting time is reached, restart from step 1.

The maximal waiting time in step 4 is introduced to upper bound the probability of losing a heralding photon before a successful BSM [147], thereby limiting the noise in the loading process.

Provided with the BSM outcomes as shown in Table I, Alice or Bob flip their bit for the outcome -1 and 1 if they used the X -basis and the Y -basis respectively. Otherwise they leave the key bit unchanged.

To get a benchmark for our simulation, we estimate the SKR K in the asymptotic limit, assuming ideal single-photon sources and efficient encoding. The key rate depends on the source repetition rate R , the expected number of writing attempts per successful Bell-state measurement N , the system yield Y , and an error correction term characterized by the quantum bit error rate e , the error correction efficiency f , and the binary Shannon entropy $h(e)$. This estimation follows the Devetak-Winter key rate formula [152]:

TABLE I. Outcomes of the BSM for matching bases. Since the phases within each basis sum to 0 or $\pm\pi$, the two possible BSM outcomes are $e^{i(\phi+\phi')} = \pm 1$. Depending on the chosen basis and the BSM outcome, Alice or Bob flip their bit or leave it as it is. After the BSM measurement is completed, both the basis choice and the BSM outcome are public information, while the bit values, encoded in the phase, are only private information of the communication parties Alice and Bob. Events with mismatched bases are discarded and therefore not displayed in this table.

Basis	ϕ	ϕ'	$e^{i(\phi+\phi')}$
XX	0	0	1
XX	0	π	-1
XX	π	0	-1
XX	π	π	1
YY	$\pi/2$	$\pi/2$	-1
YY	$\pi/2$	$-\pi/2$	1
YY	$-\pi/2$	$\pi/2$	1
YY	$-\pi/2$	$-\pi/2$	-1

$$K = \frac{R}{N} Y (1 - [(1 + f) h(e)]) . \quad (8)$$

The source repetition rate is given by $R = 1/\tau_{\text{write}}$, where τ_{write} is the time required to transfer a photonic state to the electron spin of the SiC device. The expected number of writing attempts per successful BSM, N , accounts for the time required to load both Alice’s and Bob’s states into memory and perform the BSM. This waiting time increases with transmission loss over distance but also depends on the chosen maximal waiting time.

The yield Y is the product of constant system characteristics, including the spin readout efficiency η_{read} , the BSM efficiency η_{BSM} , and the sifting ratio η_{sift} , which reflects the fraction of retained measurement results after basis reconciliation. The final factor in the SKR formula accounts for errors, where e is the quantum bit error rate and $h(e) = -e \log_2 e - (1 - e) \log_2 (1 - e)$ is the binary Shannon entropy.

C. Results and main limitations

In this section, we analyze the key parameters of SiC devices and their impact on the performance of quantum nodes in MA-MDI-QKD. In long-distance QKD, the SKR is in general constrained by link loss, as well as by a combination of system parameters such as the photon rate, time resolution, and dark count rate of single-photon detectors [153].

For memory-assisted QKD to surpass direct point-to-point QKD in SKR, the advantages of quantum memories must outweigh the costs in efficiency, processing delays, and fidelity limitations of realistic SiC devices. Therefore, we focus on analyzing the impact of key parameters

governing the performance of the asynchronous BSM, including efficiency, fidelity, communication latency, and processing time.

While we explicitly model imperfections such as finite detector quantum efficiency, dark counts, and insertion losses in optical switches and circulators, we assume ideal cavity cooperativity and spin readout fidelity for feasibility. Chiefly, we assume that the high cooperativity results in unity contrast for the two different spin states. Such approximations are suitable for the performance projections we aim for in this work. A complete set of simulation parameters is provided in App. A. Detailed calculations can be performed to refine these estimates for given experimental parameters [154].

A fundamental limitation in the system arises from the writing process into the spin memory. While spin readout fidelity is high [32], ensuring accurate measurement of stored quantum states, spin-photon entanglement fidelity is significantly lower. This results from photon loss, decoherence, and the probabilistic nature of single-photon interference, which limits the efficiency of transferring a photonic qubit into the spin memory. The loss in the memory writing process not only reduces the SKR but additionally introduces noise during memory loading process, further degrading performance.

We show with our simulation how to reduce the additional loading noise and how to increase the heralding efficiency, allowing MA-MDI-QKD outperform both point-to-point QKD and standard MDI-QKD in terms of SKR.

Memory-assisted quantum networks rely on the ability to store quantum states with high fidelity over time. In long-distance quantum links, low transmission probabilities necessitate storage to synchronize the arrival of two photons for the BSM. A noteworthy limitation of MA-MDI-QKD therefore pertains the decay of the state fidelity of the stored state due to dephasing. Dephasing is a loss of coherence due to interaction of the electron spin with the environment reducing BSM fidelity over time. The smaller the coherence time, the faster the decay, resulting in higher the noise, lower the key rates. While transferring the state from the electron spin to the long-lived nuclear spin could significantly extend the coherence time, practical limitations arise: conversion times fall within the microsecond regime, extending the writing time and thereby reducing the maximal possible source repetition rate, and nuclear spins do not couple to the cavity mode, making quantum registers impractical for this protocol. In our system, dephasing occurs continuously from the last spin state initialization to the final spin readout that concludes the BSM, including both switching and waiting times.

The influence of the coherence time T_2 on the SKR can be observed in Fig. 5. We simulated the SKR of MA-MDI-QKD for four different coherence times (100 μ s, 1 ms, 10 ms, and 100 ms), as a function of the link distance in standard telecommunication fibers (Corning SMF-28). For link lengths below 100 km, the dephasing

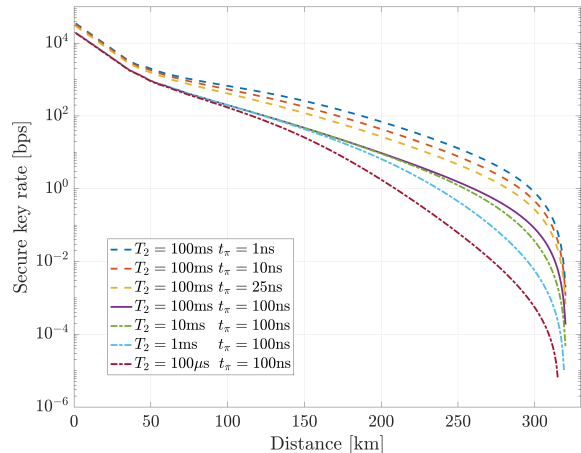


FIG. 5. MA-MDI-QKD implemented with realistic devices and varying dephasing-time T_2 (dashed) and π -pulse durations τ_π (dash-dotted). Secure key rates are plotted as a function of total separation L between Alice and Bob. Photons are transmitted over segments of $L/2$ each to the middle station via single-mode optical fiber (Corning SMF-28). The maximal waiting times are optimized for each set of parameters and each distance. For distances below 50 km the maximal waiting time is on the order of the inverse pulse rate, $1/R$. The spin is initialized after every possible time slot to write a qubit. The SKR scaling with the distance improves once waiting longer enables synchronising the signals from Alice and from Bob. Beyond 300 km the channel loss is so high, that the dark counts at 10 Hz dominate the signal-to-noise-ratio causing a drop in the SKR to zero. The secure key rates are calculated in the asymptotic limit.

has minimal impact on the SKR. For distances between 100 km and the maximal reach, where dark counts dominate, the effect of dephasing on the SKR becomes clear. For shorter coherence times, dephasing reduces the key rate substantially. Longer coherence times allow favorable scaling to be maintained over greater distances. Additionally, the sensitivity of the SKR to coherence time decreases as T_2 increases. The region where SKR scaling is dephasing-limited shifts toward longer transmission distances with increasing coherence time. To maintain high key rates at long distances ($\gtrsim 100$ km), coherence times of at least 10 ms are required.

Writing a photonic qubit into the quantum memory presents a time-consuming process when compared to the timescales of photon sources, which typically operate in the GHz regime. The primary constraint arises from the microwave pulse employed to perform unitary operations on the electron spin. The duration of a π -pulse, denoted as τ_π , determines the minimum separation between the time-bins of a qubit Δt , requiring $\Delta t \geq \tau_\pi$. Due to the probabilistic heralding measurement, photons are detected outside their initial temporal qubit space. Consequently, the time-bin separation of a single qubit also restricts the spacing between two successive time-

bin qubits. Thus, the photon repetition rate of the QKD transmitter is bounded by $1/(2\tau_\pi)$, where a typical π -pulse duration of $\tau_\pi = 100$ ns yields a maximum photon repetition rate of 5 MHz. Furthermore, the photon repetition rate incurs an additional penalty resulting from the temporal spread of the time bins, which is constrained by the bandwidth of the quantum memory as determined by the time-bandwidth product of a transform-limited pulse. As an example, for $\tau_p = 11.2$ ns, the integral in a frequency window of 100 MHz exceeds 99.95%. Including this contribution, the photon repetition rate is ultimately bounded by $1/(2\tau_\pi + 2\tau_p) = 4.5$ MHz. For $t_\pi = 10$ ns, the repetition rate increases to 23.5 MHz.

In Fig. 5, the SKR is computed for the π -pulse duration taking the values (1 ns, 10 ns, 25 ns and 100 ns). While the coherence time becomes relevant at long distances, the π -pulse length affects the SKR at every distance: A smaller π -pulse duration leads to a marked improvement for all distances, and has minor effects on the SKR scaling.

Despite this improvement, the SKR at $L = 0$ km is nearly three orders of magnitude lower than the source repetition rate. This reduction arises from the impact of the expected number of writing attempts N in the key rate formula (Equation 8). At short distances, the maximal waiting time is set to a small value to minimize loading errors. The trade-off is frequent and time-consuming memory reinitialization [147], while the error term remains close to one, as loading errors are absent and dephasing effects are minimal.

A further bottleneck of the scheme is the low heralding efficiency, constrained by an upper limit of 25%. This sets a fundamental baseline for the efficiency of the asynchronous Bell state measurement in its current implementation. A low heralding efficiency not only reduces the signal rate but also increases the noise, as the probability of undetected photon interaction with the cavity system increases. We now analyze how monitoring photon-cavity interactions that do not lead to successful heralding increases the SKR.

Two types of non-heralding photon-cavity interactions can be monitored to reduce loading noise. Firstly, the probabilistic time-bin detection has a success probability of 50%. Instead of ignoring the unsuccessful events, they can be used to trigger immediate re-initialization of the memory. This change can be implemented through an update in data collection and processing, without hardware modifications. Secondly, photons transmitted rather than reflected by the cavity can be detected.

We investigate two detection strategies for the cavity transmission: (i) A watchdog detector that registers transmission events without further analysis but triggers memory reinitialization upon detection. As shown in Fig. 6, this shortens the linear-scaling region at short fiber lengths, shifting the SKR to higher values at larger distances. (ii) Extending full time-bin detection, as used in the reflection path, to the transmission path of the cavity. While experimentally demanding and potentially

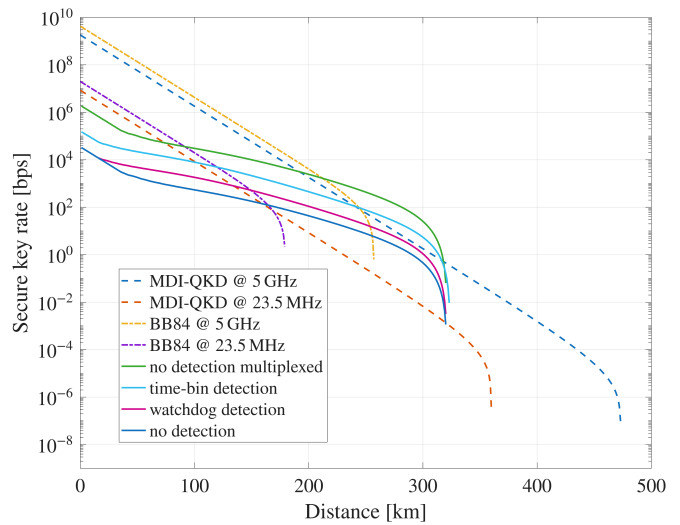


FIG. 6. MA-MDI-QKD performance with different detection strategies in cavity transmission. Secure key rates are plotted as a function of total separation L between Alice and Bob. Photons are transmitted over segments of $L/2$ each to the middle station via single-mode optical fiber (Corning SMF-28). The maximal waiting time is optimized for maximum SKR at each distance, with coherence time and π -pulse duration fixed at $T_2 = 100$ ms and $t_\pi = 10$ ns. The dark count rate is 10 Hz. As benchmarks, BB84 and MDI-QKD are shown at different photon repetition rates (23.5 MHz and 5 GHz). The SKR is calculated in the asymptotic limit. For the multiplexed curve, the no-detection curve is scaled by a multiplexing factor of 56. All detection configurations in the cavity transmission outperform protocols operating at 23.5 MHz. However, only time-bin detection and the multiplexed no-detection setup achieve higher key rates than MDI-QKD at 5 GHz for fiber lengths between 250 km and 310 km.

cost-intensive, this approach shifts the SKR to higher values across all fiber lengths, significantly enhancing system performance.

All configurations of transmission detection outperform BB84 and MDI-QKD when operated at the same repetition rate, benefiting from favorable scaling due to the asynchronous BSM. With a watchdog detector, the SKR nearly surpasses that of MDI-QKD at a state-of-the-art repetition rate of 5 GHz. Employing a second time-bin detection module in the transmission of the cavity further boosts the key rate, enabling MA-MDI-QKD to outperform both direct transmission and MDI-QKD at 5 GHz.

Independently of the detection strategy, wavelength multiplexing offers a path to higher SKR. Multiplexing techniques, commonly used in modern telecommunication networks, can be harnessed to significantly enhance quantum network transmission rates. Wavelength multiplexing in fiber networks is highly standardized, with many cost-effective, off-the-shelf components available.

The multiplexing factor of 56, which is used in Fig. 6, is derived by comparing the spectral width of the photons written to a SiC device with that of the 5 GHz system,

assuming Fourier-limited linewidths.

Multiplexing not only offers higher key rates between two fixed communication parties, but also enables the extension to networks [155] with several tens of users. Using active optical switches [156], such a network could be extended to a star topology. Pairs of user nodes are then connected to a single SiC defect at the access node, where an asynchronous BSM is performed.

Beyond the configurations we simulate, several modifications could further improve performance. First, the non-interfering detection events in time-bin measurement could speed-up memory reinitialization. These events do not herald successful writing, but they project the spin into a pure state, rendering classical readout unnecessary. The initialization time thereby reduced to the duration of a $\pi/2$ -pulse needed to restore the $|+\rangle$ state. For the spin to be projected into a pure state, the detection events of two subsequent qubits must not overlap, reducing the rate by one third. It remains to be investigated if the benefit of faster reinitialization outweighs the reduced rate due to qubit separation.

Second, the passive Mach-Zehnder interferometer used for heralding could be replaced with an actively switched version. Due to the probabilistic nature of the passive interferometer, half of the photons cannot be used to herald successful writing to the memory. Active switching, if achievable with sufficiently low insertion loss, would recover these photons and increase heralding efficiency.

Finally, it should be mentioned that photon losses could be further reduced by utilizing a different optical frequency. The photon loss in the telecommunication O-band ($\sim 0.3 \text{ dB km}^{-1}$), investigated here, is much lower than at optical wavelengths emitted by other defects [157]. Still, the band with the lowest loss, which is primarily used in optical telecommunication systems, is the C-band, with a loss of $\sim 0.2 \text{ dB km}^{-1}$. While the difference between these two bands is seemingly small, it accumulates to an order of magnitude loss difference after 100 km of propagation, providing strong motivation for the investigation of spin centres in this wavelength regime [110].

IV. enRoadmap for SiC quantum links

We now summarize the required technological steps for SiC photonics towards full deployment based on the example of repeater-extended quantum communication. In order to be competitive with other approaches, this target needs to be reached within the next decade (see Fig. 7). As underlined by the preceding calculations, this application requires high-rate spin-photon entanglement with high fidelity and long ($\gg 100 \text{ ms}$) spin coherence lifetime, with hundreds of addressable sites at each repeater node for multiplexing, to usefully exceed the rates provided by direct links.

1. Prerequisites

Regarding *materials development*, the properties of most defects in SiC can be improved by carefully controlling the properties of the host crystal [158]. Important aspects are the control of dopant density for charge state stability, a pristine crystalline structure to avoid strain inhomogeneity and undesired charge traps, and isotopic control to increase spin coherence as well as to reduce inhomogeneous broadening of the optical and spin transitions in some defects. Additionally, most if not all defects will benefit from charge depletion, which can be achieved in diode structures. A further necessity is the development of high-yield processes for the creation of thin, ultrasmooth membranes with uniform, μm -scale thickness for FP microcavities and even thinner structures for PC cavities. While proof-of-principle demonstrations of such processes have also been performed, the yield or crystal quality of these SiC membranes have not yet reached a sufficient level for large-scale deployment.

This development is necessary for all types of *optical enhancement structures* [20], apart from very few exceptions such as bullseye ring resonators, which can conceivably be implemented on bulk crystals but are not suitable for the spin-dependent reflection scheme discussed above. While defects which are spectrally and electronically stable might be utilized as emitters with Purcell or even only collection enhancement, the type of spin-photon interaction described above will be advantageous for most systems as it greatly reduces defect ionization and light-induced spectral diffusion. We underline here that defects with longer wavelength transitions benefit from lower losses and a higher tolerance to imperfections in the photonic enhancement structures: As an example, the loss due to interface roughness in FP cavities decreases with $\sigma \propto 1/\lambda^2$, leading to a corresponding increase of the enhancement. Only very few examples of photonic enhancement have been reported for SiC defects so far, making the development of these structures an important task for the scientific community.

All *candidate defect centres* will require high-fidelity spin initialization, manipulation, and readout, and will need to reach the desired coherence times. Additionally, high-yield creation of defects at predetermined positions in the crystal is highly desirable for the subsequent integration into photonic enhancement structures. In order to reduce the complexity of the multiplexing architecture, it is furthermore desirable to tune all defects at one repeater site to the same optical frequency so as to achieve indistinguishability. For most defects, this requirement implies tuning by strain or electrostatic means. Together with the requirement for fast individual spin control, this necessity implies a high degree of integration with multiple wire structures on the SiC surface, for which stringent limits on the power dissipation and conductive thermal load are given by the cooling power of the cryogenic environment. This, in turn, hints at the necessity for resonantly enhanced and/or superconduct-

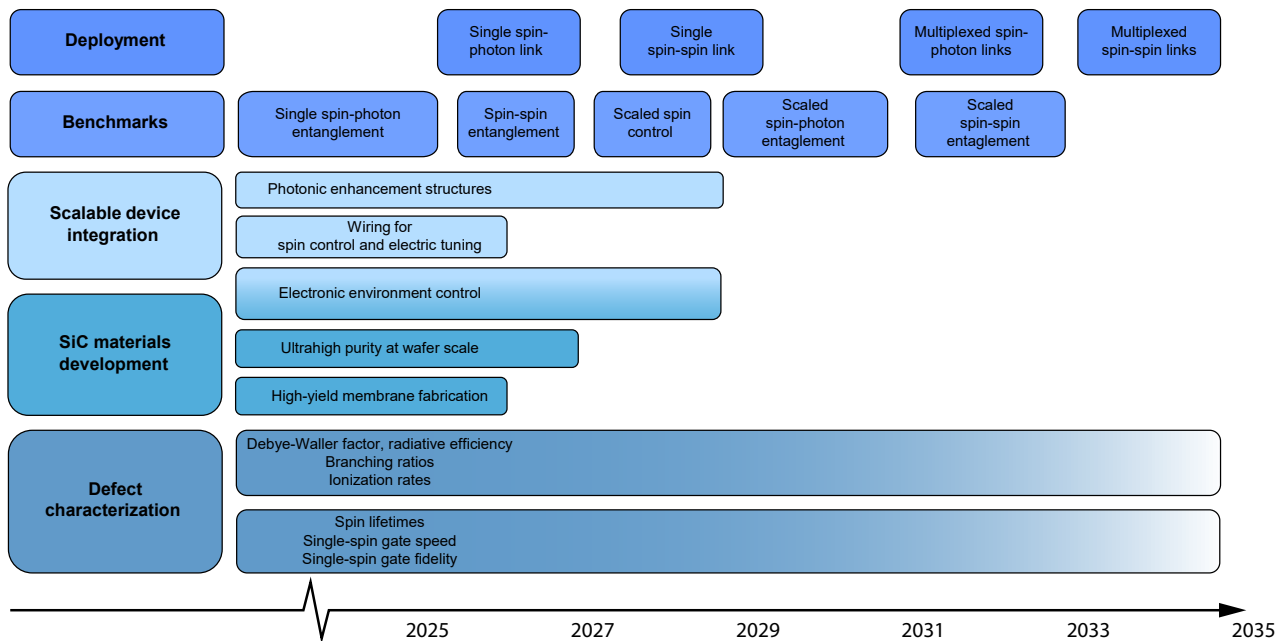


FIG. 7. Roadmap for deployment of high-performance quantum links based on SiC photonics in the next decade. Bar ends indicate when technological developments (materials, integration) are expected to have reached a level suitable for large-scale deployment. Similarly, bar ends for benchmarks indicate when a performance level sufficient for deployment on metropolitan-scale links is achieved. Defect identification, characterization, and development is expected to lead to continued improvements throughout this evolution.

ing spin control structures.

Many of the postulated requirements imply the use of *cryogenic infrastructure* for all candidate defects, though only vanadium is known to require temperatures < 1 K for sufficiently long spin relaxation lifetimes, while impressive coherence times have been achieved with other defect systems at around 4 K.

Finally, *wavelength conversion* will be necessary for most of the known defects in SiC. The development of compact, scalable, and efficient converters will thus be necessary for most candidate defects. Successful proof-of-principle demonstrations have been achieved, but engineering a solution that is deployable at scale remains an outstanding task.

2. Applications

Photonic quantum links with memory units are broadly seen as having four distinct applications, which pose slightly different requirements:

Repeaters for quantum key distribution that are integrated in a global network additionally require an efficient interface to space-based quantum communication systems, which currently operate at visible wavelengths or in the telecom C-band.

Photonicallly connected qubits or qudits within spin-based quantum computers can be envisioned

without wavelength conversion or frequency multiplexing. Fault-tolerant architectures, however, place even greater demands on yield, scalability, coherence, and fidelity of the SPI's. Additionally, they can benefit more strongly from nuclear spin ancillae than simple communication protocols. Quantum computing architectures based on small quantum processing units connected by a photonic channel [159], all integrated on a single SiC chip including elements such as waveguides, Bragg filters, electrically-controlled optical modulators for routing, etc., can be envisioned.

Further applications will be entanglement distribution for other *networked quantum computers* and entanglement distribution for *networked quantum sensors*. For these, interfacing between the qubits or quantum sensors and the SPI needs to be developed.

3. Prioritization

These differences notwithstanding, the overall set of requirements allows to set priority levels for development of different aspects of the technology. We focus here on aspects which are specifically connected to SiC devices, thereby excluding wavelength conversion and cryogenic infrastructure, to which advances in SiC photonics cannot contribute directly. The highest priority should be given to materials development aspects, particularly the

development of wafer-scale membranes. Most of these are additionally beneficial to the SiC industry and to emerging applications of classical SiC photonics, thereby providing the highest incentives overall. The next priority is the selection of the most suitable defect for deployment, as this determines the requirements for photonic enhancement and interoperability with telecom networks. As several defects currently under study present advantageous features, this decision can only be taken at a later stage of technological development. Nonetheless, several performance parameters need to be ascertained precisely along this path, including the Debye-Waller factor, radiative efficiency, and transition branching ratios, the spin relaxation and coherence lifetimes, the operation temperature, as well as any limitations on the single-spin initialization, readout, as well as gate times and fidelities which could limit the SPI performance. This type of characterization can be expected to exclude several defects from applications in quantum photonics. However, as new candidate defects continue to emerge, this task will remain ongoing beyond the deployment of the first devices.

For SPI benchmarking, each defect with sufficient performance parameters needs to be incorporated in a photonic enhancement structure, replete with all control wiring and potentially with SiC diode structures. Aside from the enhancement factor, the main emphasis in this development must be placed on scalability, as vast numbers of SPI's will be required for all quantum technology applications. A large part of these technological aspects is common to all defects and should therefore be performed in parallel to the detailed characterization of spin centres.

Since different applications and protocols place differing requirements on the performance of the SPI, a global benchmark cannot be defined. Nonetheless, certain performance indicators are common to most settings. A possible baseline benchmark which encapsulates many of the stated requirements is the product of the spin-photon entanglement rate and the spin coherence lifetime at telecom wavelength and after fiber coupling. The next benchmark level is the product of rate and lifetime of spin-spin entanglement with two such units, which subsumes aspects such as indistinguishability and synchronization. Both of these benchmarks need to be defined with a threshold fidelity, or be scaled appropriately for a chosen protocol.

4. *Timeline*

For these developments to take place within the next decade, a concerted effort by the SiC photonics community with strong industrial participation will be required. The payoff, however, will be large for all involved stakeholders, and will provide technological developments with beneficial effects far beyond the science and technology domains. While ambitious, the timeline for these devel-

opments can be achieved assuming continued growth in support from governments and continued advances in the burgeoning SiC industry.

V. **enSummary**

We have provided an overview of SiC photonics using spin centres for quantum links. These devices have applications in quantum computing, secure key distribution, and as entanglement links for distributed quantum computation and sensing. Using memory-assisted QKD as an example, we have investigated the key parameters which determine the performance of such links.

We have undertaken a comprehensive analysis of the key parameters of SiC devices and their impact on the performance of quantum nodes in the context of memory-assisted measurement-device-independent-QKD. We opted for this particular QKD protocol as it provides a practical benchmark for examining the performance of a single quantum memory by focusing on a single parameter, the secure key rate. Importantly, the implementation of this protocol with SiC devices includes all essential building blocks of large-scale repeater networks. Our investigation has revealed several crucial factors that influence the secure key rate over long communication distances, shedding light on both the potential and limitations of spin centers in SiC. Furthermore, the SiC platform's compatibility with wavelength multiplexing enables scaling to multi-user networks, as discussed in Section III C.

Quantum repeater networks are the ultimate goal for long-distance quantum communication and the SiC platform is a strong candidate for serving this purpose. This vision can only be realized once a single quantum repeater node outperforms point-to-point quantum communication. Only then, quantum repeater networks with several quantum repeater nodes will prove beneficial in quantum communication and might be deployed in the field. This should also guide the experimental efforts in SiC-based SPI's. Therefore, the first milestone on the roadmap towards a large-scale quantum repeater network is the demonstration of the single-node [27] or two-node [17, 18] scenario.

Beyond beating the repeaterless bound [160] per channel use [27, 143], we benchmark SiC devices with existing QKD technologies, which, for example, allow higher photon repetition rates compared to current specifications of CQED devices. This practical approach allows us to make statements about the operational capability of SiC-based quantum memories in real-world quantum networks. In particular, the results highlight the need for multiplexing in order to achieve competitive secret key rates. Scalability in SPI production and interconnects is therefore a requirement for any quantum repeater technology based on spin-photon interfaces.

Another usecase is the deployment of SiC devices for end nodes in quantum networks. The quantum memo-

ries in end nodes delay the read-out of photonic quantum states or re-emit stored states after certain time intervals for various quantum information processing tasks. End nodes therefore have a different set of requirements compared to repeater nodes. As an example, the transfer to nuclear spins is a good option to increase the storage time of end nodes, even though in-depth comparison to other quantum memory platforms is necessary to evaluate the deployability of defects in SiC for this usecase.

These considerations allow to define a path towards deployment of SiC photonics for high-performance quantum links, outlined in Sec.IV. We project that, with a

concerted effort of the scientific community and the SiC industry, it will be possible to achieve this goal within a decade.

VI. Acknowledgements

This work was funded by the European Union under grant agreements No 862721 (QuanTELCO) and 101186889 (QuSPARC). We acknowledge support from the Austrian Research Promotion Agency project under projects FFG FO999914034 (SPQV) and FO999921415 (VANESSA_QC).

-
- [1] S. Wehner, D. Elkouss, and R. Hanson, *Science* **362**, eaam9288 (2018).
 - [2] Z. Zhang and Q. Zhuang, *Quantum Science and Technology* **6**, 043001 (2021).
 - [3] J. L. Park, *Foundations of physics* **1**, 23 (1970).
 - [4] W. K. Wootters and W. H. Zurek, *Nature* **299**, 802 (1982).
 - [5] C.-Y. Lu, Y. Cao, C.-Z. Peng, and J.-W. Pan, *Rev. Mod. Phys.* **94**, 035001 (2022).
 - [6] S.-K. Liao, W.-Q. Cai, J. Handsteiner, B. Liu, J. Yin, L. Zhang, D. Rauch, M. Fink, J.-G. Ren, W.-Y. Liu, Y. Li, Q. Shen, Y. Cao, F.-Z. Li, J.-F. Wang, Y.-M. Huang, L. Deng, T. Xi, L. Ma, T. Hu, L. Li, N.-L. Liu, F. Koidl, P. Wang, Y.-A. Chen, X.-B. Wang, M. Steindorfer, G. Kirchner, C.-Y. Lu, R. Shu, R. Ursin, T. Scheidl, C.-Z. Peng, J.-Y. Wang, A. Zeilinger, and J.-W. Pan, *Phys. Rev. Lett.* **120**, 030501 (2018).
 - [7] S. Ecker, J. Pseiner, J. Piris, and M. Bohmann, in *International Conference on Space Optics — ICSO 2022*, Vol. 12777, edited by K. Minoglou, N. Karafolas, and B. Cugny, International Society for Optics and Photonics (SPIE, 2023) p. 1277727.
 - [8] H.-J. Briegel, W. Dür, J. I. Cirac, and P. Zoller, *Physical Review Letters* **81**, 5932 (1998).
 - [9] D. P. DiVincenzo, *Fortschritte der Physik: Progress of Physics* **48**, 771 (2000).
 - [10] D. M. Lukin, M. A. Guidry, and J. Vučković, *PRX Quantum* **1**, 020102 (2020).
 - [11] A. Dréau, A. Tchebotareva, A. E. Mahdaoui, C. Bonato, and R. Hanson, *Phys. Rev. Appl.* **9**, 064031 (2018).
 - [12] A. Tchebotareva, S. L. Hermans, P. C. Humphreys, D. Voigt, P. J. Harmsma, L. K. Cheng, A. L. Verlaan, N. Dijkhuizen, W. de Jong, A. Dréau, and R. Hanson, *Physical Review Letters* **123** (2019), 10.1103/physrevlett.123.063601.
 - [13] J. V. Rakonjac, D. Lago-Rivera, A. Seri, M. Mazzer, S. Grandi, and H. de Riedmatten, *Phys. Rev. Lett.* **127**, 210502 (2021).
 - [14] K. Hammerer, A. S. Sørensen, and E. S. Polzik, *Rev. Mod. Phys.* **82**, 1041 (2010).
 - [15] S. T. Y. Ilmaz, P. Fallahi, and A. Imamoğlu, *Phys. Rev. Lett.* **105**, 033601 (2010).
 - [16] P. Lodahl, *Quantum Science and Technology* **3**, 013001 (2017).
 - [17] D. Lago-Rivera, S. Grandi, J. V. Rakonjac, A. Seri, and H. de Riedmatten, *Nature* **594**, 37 (2021).
 - [18] X. Liu, J. Hu, Z. F. Li, X. Li, P. Y. Li, P. J. Liang, Z. Q. Zhou, C. F. Li, and G. C. Guo, *Nature* **594**, 41 (2021).
 - [19] V. Krutyanskiy, M. Galli, V. Krcmarsky, S. Baier, D. A. Fioretto, Y. Pu, A. Mazloom, P. Sekatski, M. Canteri, M. Teller, J. Schupp, J. Bate, M. Meraner, N. Sangouard, B. P. Lanyon, and T. E. Northup, *Phys. Rev. Lett.* **130**, 050803 (2023).
 - [20] S. Castelletto, A. Peruzzo, C. Bonato, B. C. Johnson, M. Radulaski, H. Ou, F. Kaiser, and J. Wrachtrup, *ACS Photonics* **9**, 1434 (2022).
 - [21] Y. Zhou, J. Tan, H. Hu, S. Hua, C. Jiang, B. Liang, T. Bao, X. Nie, S. Xiao, D. Lu, J. Wang, and Q. Song, *Applied Physics Reviews* **12** (2025).
 - [22] D. J. Christle, P. V. Klimov, C. F. de las Casas, K. Szász, V. Ivády, V. Jokubavicius, J. Ul Hassan, M. Syväjärvi, W. F. Koehl, T. Ohshima, N. T. Son, E. Jánzén, A. Gali, and D. D. Awschalom, *Physical Review X* **7**, 021046 (2017).
 - [23] R. Vasconcelos, S. Reisenbauer, C. Salter, G. Wachter, D. Wirtitsch, J. Schmiedmayer, P. Walther, and M. Trupke, *npj Quantum Information* **6** (2020), 10.1038/s41534-019-0236-x.
 - [24] J. Bader, H. Arianfar, A. Peruzzo, and S. Castelletto, *npj Nanophotonics* **1**, 29 (2024).
 - [25] Z.-X. He, G. Thiering, R.-J. Liang, J.-Y. Zhou, S. Ren, W.-X. Lin, Z.-H. Hao, Q.-C. Hu, J.-F. Wang, A. Gali, *et al.*, arXiv preprint arXiv:2602.06421 (2026).
 - [26] C. Panayi, M. Razavi, X. Ma, and N. Lütkenhaus, *New Journal of Physics* **16** (2014), 10.1088/1367-2630/16/4/043005.
 - [27] M. K. Bhaskar, R. Riedinger, B. Machielse, D. S. Levonian, C. T. Nguyen, E. N. Knall, H. Park, D. Englund, M. Lončar, D. D. Sukachev, and M. D. Lukin, *Nature* **580**, 60 (2020).
 - [28] M. Pompili, S. L. Hermans, S. Baier, H. K. Beukers, P. C. Humphreys, R. N. Schouten, R. F. Vermeulen, M. J. Tiggelman, L. dos Santos Martins, B. Dirkse, *et al.*, *Science* **372**, 259 (2021).
 - [29] E. Bersin, M. Sutula, Y. Q. Huan, A. Suleymanzade, D. R. Assumpcao, Y.-C. Wei, P.-J. Stas, C. M. Knaut, E. N. Knall, C. Langrock, *et al.*, arXiv preprint arXiv:2307.08619 (2023).

- [30] B.-W. Lu, C.-W. Yang, R.-Q. Wang, B.-F. Gao, Y.-Z. Zhen, Z.-G. Wang, J.-K. Shi, Z.-Q. Ren, T. A. Hahn, E. Y.-Z. Tan, *et al.*, *Science* **391**, 592 (2026).
- [31] W.-Z. Liu, Y.-B. Zhou, J.-P. Chen, B. Wang, A. Teng, X.-W. Han, G.-C. Liu, Z.-J. Zhang, Y. Yang, F.-G. Liu, *et al.*, *Nature*, 1 (2026).
- [32] K. Azuma, S. E. Economou, D. Elkouss, P. Hilaire, L. Jiang, H.-K. Lo, and I. Tzitrin, *Rev. Mod. Phys.* **95**, 045006 (2023).
- [33] E. Janzén, A. Henry, J. P. Bergman, A. Ellison, and B. Magnusson, *Materials Science in Semiconductor Processing Advanced Characterisation of Semiconductor Materials*, **4**, 181 (2001).
- [34] A. Gali, A. Gällström, N. T. Son, and E. Janzén, *Materials Science Forum* **645-648**, 395 (2010).
- [35] D. J. Christle, A. L. Falk, P. Andrich, P. V. Klimov, J. U. Hassan, N. T. Son, E. Janzén, T. Ohshima, and D. D. Awschalom, *Nature Materials* **14**, 160 (2015).
- [36] M. Widmann, S.-Y. Lee, T. Rendler, N. T. Son, H. Fedder, S. Paik, L.-P. Yang, N. Zhao, S. Yang, I. Booker, A. Denisenko, M. Jamali, S. A. Momenzadeh, I. Gerhardt, T. Ohshima, A. Gali, E. Janzén, and J. Wrachtrup, *Nature Materials* **14**, 164 (2015).
- [37] J.-F. Wang, F.-F. Yan, Q. Li, Z.-H. Liu, H. Liu, G.-P. Guo, L.-P. Guo, X. Zhou, J.-M. Cui, J. Wang, Z.-Q. Zhou, X.-Y. Xu, J.-S. Xu, C.-F. Li, and G.-C. Guo, *Physical Review Letters* **124**, 223601 (2020).
- [38] G. Wolfowicz, C. P. Anderson, B. Diler, O. G. Poluektov, F. J. Heremans, and D. D. Awschalom, *Science Advances* **6**, eaaz1192 (2020).
- [39] P. Cilibrizzi, M. J. Arshad, B. Tissot, N. T. Son, I. G. Ivanov, T. Astner, P. Koller, M. Ghezellou, J. Ul-Hassan, D. White, C. Bekker, G. Burkard, M. Trupke, and C. Bonato, *Nature Communications* **14**, 8448 (2023).
- [40] L. Gordon, A. Janotti, and C. G. Van de Walle, *Physical Review B* **92**, 045208 (2015).
- [41] H. J. von Bardeleben, J. L. Cantin, A. Csóré, A. Gali, E. Rauls, and U. Gerstmann, *Physical Review B* **94**, 121202 (2016).
- [42] A. Csóré, H. J. von Bardeleben, J. L. Cantin, and A. Gali, *Physical Review B* **96**, 085204 (2017).
- [43] J.-F. Wang, Z.-H. Liu, F.-F. Yan, Q. Li, X.-G. Yang, L. Guo, X. Zhou, W. Huang, J.-S. Xu, C.-F. Li, and G.-C. Guo, *ACS Photonics* **7**, 1611 (2020).
- [44] Z. Mu, S. A. Zargaleh, H. J. von Bardeleben, J. E. Fröch, M. Nonahal, H. Cai, X. Yang, J. Yang, X. Li, I. Aharonovich, and W. Gao, *Nano Letters* **20**, 6142 (2020).
- [45] F. F. Murzakhanov, B. V. Yavkin, G. V. Mamin, S. B. Orlinskii, H. J. von Bardeleben, T. Biktagirov, U. Gerstmann, and V. A. Soltamov, *Physical Review B* **103**, 245203 (2021).
- [46] H. Jurgen von Bardeleben, J.-L. Cantin, U. Gerstmann, W. G. Schmidt, and T. Biktagirov, *Nano Letters* **21**, 8119 (2021).
- [47] T. Narahara, S.-i. Sato, K. Kojima, Y. Hijikata, and T. Ohshima, *Applied Physics Express* **14**, 021004 (2021).
- [48] J. Schneider, H. D. Müller, K. Maier, W. Wilkening, F. Fuchs, A. Dörnen, S. Leibenzeder, and R. Stein, *Applied Physics Letters* **56**, 1184 (1990).
- [49] B. Kaufmann, A. Dörnen, and F. S. Ham, *Materials Science Forum* **196-201**, 707 (1995).
- [50] J. Baur, M. Kunzer, and J. Schneider, *physica status solidi (a)* **162**, 153 (1997).
- [51] A. L. Falk, P. V. Klimov, V. Ivády, K. Szász, D. J. Christle, W. Koehl, A. Gali, and D. D. Awschalom, *Physical Review Letters* **114**, 247603 (2015).
- [52] V. Ivády, P. V. Klimov, K. C. Miao, A. L. Falk, D. J. Christle, K. Szász, I. A. Abrikosov, D. D. Awschalom, and A. Gali, *Physical Review Letters* **117**, 220503 (2016).
- [53] A. Bourassa, C. P. Anderson, K. C. Miao, M. Onizhuk, H. Ma, A. L. Crook, H. Abe, J. Ul-Hassan, T. Ohshima, N. T. Son, G. Galli, and D. D. Awschalom, *Nature Materials* **19**, 1319 (2020).
- [54] L. Robledo, L. Childress, H. Bernien, B. Hensen, P. F. A. Alkemade, and R. Hanson, *Nature* **477**, 574 (2011).
- [55] R. Nagy, M. Niethammer, M. Widmann, Y.-C. Chen, P. Udvarhelyi, C. Bonato, J. U. Hassan, R. Karhu, I. G. Ivanov, N. T. Son, J. R. Maze, T. Ohshima, O. O. Soykal, A. Gali, S.-Y. Lee, F. Kaiser, and J. Wrachtrup, *Nature Communications* **10**, 1954 (2019).
- [56] B. Tissot, M. Trupke, P. Koller, T. Astner, and G. Burkard, *Physical Review Research* **4**, 033107 (2022).
- [57] C. Yin, M. Rancic, G. G. de Boo, N. Stavrias, J. C. McCallum, M. J. Sellars, and S. Rogge, *Nature* **497**, 91 (2013).
- [58] Q. Zhang, Y. Guo, W. Ji, M. Wang, J. Yin, F. Kong, Y. Lin, C. Yin, F. Shi, Y. Wang, and J. Du, *Nature Communications* **12**, 1529 (2021).
- [59] C. P. Anderson, E. O. Glen, C. Zeledon, A. Bourassa, Y. Jin, Y. Zhu, C. Vorwerk, A. L. Crook, H. Abe, J. Ul-Hassan, T. Ohshima, N. T. Son, G. Galli, and D. D. Awschalom, *Science Advances* **8**, eabm5912 (2022).
- [60] R.-Z. Fang, X.-Y. Lai, T. Li, R.-Z. Su, B.-W. Lu, C.-W. Yang, R.-Z. Liu, Y.-K. Qiao, C. Li, Z.-G. He, J. Huang, H. Li, L.-X. You, Y.-H. Huo, X.-H. Bao, and J.-W. Pan, “Experimental generation of spin-photon entanglement in silicon carbide,” (2023), arXiv:2311.17455 [quant-ph].
- [61] T. H. Taminiau, J. J. T. Wagenaar, T. van der Sar, F. Jelezko, V. V. Dobrovitski, and R. Hanson, *Phys. Rev. Lett.* **109**, 137602 (2012).
- [62] C. E. Bradley, J. Randall, M. H. Abobeih, R. C. Berrevoets, M. J. Degen, M. A. Bakker, M. Markham, D. J. Twitchen, and T. H. Taminiau, *Phys. Rev. X* **9**, 031045 (2019).
- [63] J. Cramer, N. Kalb, M. A. Rol, B. Hensen, M. S. Blok, M. Markham, D. J. Twitchen, R. Hanson, and T. H. Taminiau, *Nature Communications* **7**, 11526 (2016).
- [64] S. K. Parthasarathy, B. Kallinger, F. Kaiser, P. Berwian, D. B. Dasari, J. Friedrich, and R. Nagy, *Phys. Rev. Appl.* **19**, 034026 (2023).
- [65] E. Janzén, A. Gali, P. Carlsson, A. Gällström, B. Magnusson, and N. Son, *Physica B: Condensed Matter* **404**, 4354 (2009).
- [66] V. Ivády, J. Davidsson, N. T. Son, T. Ohshima, I. A. Abrikosov, and A. Gali, *Physical Review B* **96**, 161114 (2017).
- [67] P. G. Baranov, A. P. Bundakova, A. A. Soltamova, S. B. Orlinskii, I. V. Borovykh, R. Zondervan, R. Verberk, and J. Schmidt, *Physical Review B* **83**, 125203 (2011).
- [68] A. Gali, *Journal of Materials Research* **27**, 897 (2012).
- [69] D. Riedel, F. Fuchs, H. Kraus, S. VÁřth, A. Sperlich, V. Dyakonov, A. A. Soltamova, P. G. Baranov, V. A.

- Ilyin, and G. V. Astakhov, *Physical Review Letters* **109**, 226402 (2012).
- [70] V. A. Soltamov, A. A. Soltamova, P. G. Baranov, and I. I. Proskuryakov, *Physical Review Letters* **108**, 226402 (2012).
- [71] O. O. Soykal, P. Dev, and S. E. Economou, *Physical Review B* **93**, 081207 (2016).
- [72] O. O. Soykal and T. L. Reinecke, *Physical Review B* **95**, 081405 (2017).
- [73] W. Dong, M. W. Doherty, and S. E. Economou, *Physical Review B* **99**, 184102 (2019).
- [74] M. Widmann, M. Niethammer, D. Y. Fedyanin, I. A. Khramtsov, T. Rendler, I. D. Booker, J. Ul Hassan, N. Morioka, Y.-C. Chen, I. G. Ivanov, *et al.*, *Nano letters* **19**, 7173 (2019).
- [75] J.-F. Wang, F.-F. Yan, Q. Li, Z.-H. Liu, J.-M. Cui, Z.-D. Liu, A. Gali, J.-S. Xu, C.-F. Li, and G.-C. Guo, *Nature Communications* **12**, 3223 (2021).
- [76] N. T. Son, P. Carlsson, J. ul Hassan, E. Janzén, T. Umeda, J. Isoya, A. Gali, M. Bockstedte, N. Morishita, T. Ohshima, and H. Itoh, *Physical Review Letters* **96**, 055501 (2006).
- [77] A. Gali, *physica status solidi (b)* **248**, 1337 (2011).
- [78] W. F. Koehl, B. B. Buckley, F. J. Heremans, G. Calusine, and D. D. Awschalom, *Nature* **479**, 84 (2011).
- [79] V. Ivády, J. Davidsson, N. Deegan, A. L. Falk, P. V. Klimov, S. J. Whiteley, S. O. Hruszkewycz, M. V. Holt, F. J. Heremans, N. T. Son, D. D. Awschalom, I. A. Abrikosov, and A. Gali, *Nature Communications* **10**, 5607 (2019).
- [80] Q. Li, J.-F. Wang, F.-F. Yan, J.-Y. Zhou, H.-F. Wang, H. Liu, L.-P. Guo, X. Zhou, A. Gali, Z.-H. Liu, *et al.*, *National Science Review* **9**, nwab122 (2022).
- [81] L. Spindlberger, A. Csóré, G. Thiering, S. Putz, R. Karhu, J. Hassan, N. Son, T. Fromherz, A. Gali, and M. Trupke, *Physical Review Applied* **12** (2019), 10.1103/physrevapplied.12.014015.
- [82] H. Sternschulte, K. Thonke, R. Sauer, P. C. Münzinger, and P. Michler, *Physical Review B* **50**, 14554 (1994).
- [83] J. P. Goss, R. Jones, S. J. Breuer, P. R. Briddon, and S. Öberg, *Physical Review Letters* **77**, 3041 (1996).
- [84] E. Neu, D. Steinmetz, J. Riedrich-Müller, S. Gsell, M. Fischer, M. Schreck, and C. Becher, *New Journal of Physics* **13**, 025012 (2011).
- [85] A. Gali and J. R. Maze, *Physical Review B* **88**, 235205 (2013).
- [86] C. Hepp, T. Müller, V. Waselowski, J. N. Becker, B. Pingault, H. Sternschulte, D. Steinmüller-Nethl, A. Gali, J. R. Maze, M. Atatüre, and C. Becher, *Physical Review Letters* **112**, 036405 (2014).
- [87] G. Thiering and A. Gali, *Physical Review X* **8**, 021063 (2018).
- [88] M. Ruf, N. H. Wan, H. Choi, D. Englund, and R. Hanson, *Journal of Applied Physics* **130**, 070901 (2021).
- [89] B. Pingault, J. N. Becker, C. H. H. Schulte, C. Arend, C. Hepp, T. Godde, A. I. Tartakovskii, M. Markham, C. Becher, and M. Atatüre, *Physical Review Letters* **113**, 263601 (2014).
- [90] L. J. Rogers, K. D. Jahnke, M. H. Metsch, A. Sipahigil, J. M. Binder, T. Teraji, H. Sumiya, J. Isoya, M. D. Lukin, P. Hemmer, and F. Jelezko, *Physical Review Letters* **113**, 263602 (2014).
- [91] J. N. Becker, J. Görlitz, C. Arend, M. Markham, and C. Becher, *Nature Communications* **7**, 13512 (2016).
- [92] B. Pingault, D.-D. Jarausch, C. Hepp, L. Klintberg, J. N. Becker, M. Markham, C. Becher, and M. Atatüre, *Nature Communications* **8**, 15579 (2017).
- [93] D. D. Sukachev, A. Sipahigil, C. T. Nguyen, M. K. Bhaskar, R. E. Evans, F. Jelezko, and M. D. Lukin, *Physical Review Letters* **119**, 223602 (2017).
- [94] J. N. Becker, B. Pingault, D. Groß, M. Gündoğan, N. Kukharchyk, M. Markham, A. Edmonds, M. Atatüre, P. Bushev, and C. Becher, *Physical Review Letters* **120**, 053603 (2018).
- [95] Y.-I. Sohn, S. Meesala, B. Pingault, H. A. Atikian, J. Holzgrafe, M. Gündoğan, C. Stavrakas, M. J. Stanley, A. Sipahigil, J. Choi, M. Zhang, J. L. Pacheco, J. Abraham, E. Bielejec, M. D. Lukin, M. Atatüre, and M. Lončar, *Nature Communications* **9**, 1 (2018).
- [96] B. Machielse, S. Bogdanovic, S. Meesala, S. Gauthier, M. J. Burek, G. Joe, M. Chalupnik, Y. I. Sohn, J. Holzgrafe, R. E. Evans, C. Chia, H. Atikian, M. K. Bhaskar, D. D. Sukachev, L. Shao, S. Maity, M. D. Lukin, and M. Loncar, *Physical Review X* **9**, 031022 (2019).
- [97] E. Bersin, M. Sutula, Y. Q. Huan, A. Suleymanzade, D. R. Assumpcao, Y.-C. Wei, P.-J. Stas, C. M. Knaut, E. N. Knall, C. Langrock, N. Sinclair, R. Murphy, R. Riedinger, M. Yeh, C. Xin, S. Bandyopadhyay, D. D. Sukachev, B. Machielse, D. S. Levoniani, M. K. Bhaskar, S. Hamilton, H. Park, M. Lončar, M. M. Fejer, P. B. Dixon, D. R. Englund, and M. D. Lukin, *PRX Quantum* **5**, 010303 (2024).
- [98] B. Tissot and G. Burkard, *Phys. Rev. B* **104**, 064102 (2021).
- [99] C. M. Gilardoni, I. Ion, F. Hendriks, M. Trupke, and C. H. v. d. Wal, *New Journal of Physics* **23**, 083010 (2021).
- [100] A. Csóré and A. Gali, *Physical Review B* **102**, 241201 (2020).
- [101] T. Astner, P. Koller, C. M. Gilardoni, J. Hendriks, N. T. Son, I. G. Ivanov, J. U. Hassan, C. H. van der Wal, and M. Trupke, “Vanadium in Silicon Carbide: Telecom-ready spin centres with long relaxation lifetimes and hyperfine-resolved optical transitions,” (2022), arXiv:2206.06240.
- [102] P. Koller, T. Astner, B. Tissot, G. Burkard, and M. Trupke, “Strain-enabled control of the vanadium qudit in silicon carbide,” (2025), arXiv:2501.05896 [quant-ph].
- [103] J. Hendriks, C. M. Gilardoni, C. Adambukulam, A. Laucht, and C. H. van der Wal, “Coherent spin dynamics of hyperfine-coupled vanadium impurities in silicon carbide,” (2022), arXiv:2210.09942.
- [104] C. Bekker, M. J. Arshad, P. Cilibrizzi, C. Nikolatos, P. Lomax, G. S. Wood, R. Cheung, W. Knolle, N. Ross, B. Gerardot, and C. Bonato, *Applied Physics Letters* **122**, 173507 (2023).
- [105] D. O. Bracher and E. L. Hu, *Nano Letters* **15**, 6202 (2015).
- [106] M. Radulaski, M. Widmann, M. Niethammer, J. L. Zhang, S.-Y. Lee, T. Rendler, K. G. Lagoudakis, N. T. Son, E. Janzén, T. Ohshima, J. Wrachtrup, and J. Vučković, *Nano Letters* **17**, 1782 (2017).
- [107] C. Babin, R. Stöhr, N. Morioka, T. Linkewitz, T. Steidl, R. Wörnle, D. Liu, E. Hesselmeier, V. Vorobyov, A. Denisenko, M. Hentschel, C. Gobert, P. Berwian, G. V. Astakhov, W. Knolle, S. Majety, P. Saha, M. Radulaski, N. T. Son, J. Ul-Hassan, F. Kaiser, and

- J. Wrachtrup, *Nature Materials* **21**, 67 (2022).
- [108] C. P. Anderson, A. Bourassa, K. C. Miao, G. Wolfowicz, P. J. Mintun, A. L. Crook, H. Abe, J. Ul Hassan, N. T. Son, T. Ohshima, and D. D. Awschalom, *Science* **366**, 1225 (2019).
- [109] D. Shafizadeh, V. Jokubavicius, K. Murata, H. Tsuchida, P. Udvarhelyi, G. Bian, O. Lang, M. Karaman, D. H. Enriquez, M. Brehm, *et al.*, *Physical Review B* **113**, 075201 (2026).
- [110] A. N. Anisimov, A. V. Mathews, K. Mavridou, U. Kentsch, M. Helm, and G. V. Astakhov, *Optics Express* **33**, 54285 (2025).
- [111] X. She, A. Q. Huang, O. Lucia, and B. Ozpineci, *IEEE Transactions on Industrial Electronics* **64**, 8193 (2017).
- [112] T. Kimoto, *Proceedings of the Japan Academy, Series B* **98**, 161 (2022).
- [113] F. L. Via, D. Alquier, F. Giannazzo, T. Kimoto, P. Neudeck, H. Ou, A. Roncaglia, S. E. Sadow, and S. Tudisco, *Micromachines* **14**, 1200 (2023).
- [114] H. Ou, X. Shi, Y. Lu, M. Kollmuss, J. Steiner, V. Tabouret, M. Syväjärvi, P. Wellmann, and D. Chaussende, *Materials* **16**, 1014 (2023).
- [115] S. Wang, M. Zhan, G. Wang, H. Xuan, W. Zhang, C. Liu, C. Xu, Y. Liu, Z. Wei, and X. Chen, *Laser Photonics Rev.* **7**, 831 (2013).
- [116] Y. Zheng, M. Pu, A. Yi, X. Ou, and H. Ou, *Opt. Lett.* **44**, 5784 (2019).
- [117] Y. Zheng, M. Pu, A. Yi, B. Chang, T. You, K. Huang, A. N. Kamel, M. R. Henriksen, A. A. Jørgensen, X. Ou, *et al.*, *Opt. Express* **27**, 13053 (2019).
- [118] H. Sato, M. Abe, I. Shoji, J. Suda, and T. Kondo, *J. of the Opt. Society of America B* **26**, 1892 (2009).
- [119] M. A. Guidry, K. Y. Yang, D. M. Lukin, A. Markosyan, J. Yang, M. M. Fejer, and J. Vučković, *Optica* **7**, 1139 (2020).
- [120] X. Shi, Y. Lu, and H. Ou, *Optics Letters* **48**, 616 (2023).
- [121] X. Shi, W. Fan, Y. Lu, A. K. Hansen, M. Chi, A. Yi, X. Ou, K. Rottwitt, and H. Ou, *APL Photonics* **6** (2021), 10.1063/5.0053296.
- [122] A. Yi, Y. Zheng, H. Huang, J. Lin, Y. Yan, T. You, K. Huang, S. Zhang, C. Shen, M. Zhou, W. Huang, J. Zhang, S. Zhou, H. Ou, and X. Ou, *Optical Materials* **107**, 109990 (2020).
- [123] Y. Zheng, M. Pu, A. Yi, X. Ou, and H. Ou, *Optics Letters* **44**, 5784 (2019).
- [124] I. Chatzopoulos, F. Martini, R. Cernansky, and A. Politi, *ACS Photonics* **6**, 1826 (2019).
- [125] A. Faraon, C. Santori, Z. Huang, K.-M. C. Fu, V. M. Acosta, D. Fattal, and R. G. Beausoleil, *New Journal of Physics* **15**, 025010 (2013).
- [126] A. Reiserer and G. Rempe, *Rev. Mod. Phys.* **87**, 1379 (2015).
- [127] J. Fait, S. Putz, G. Wachter, J. Schalko, U. Schmid, M. Arndt, and M. Trupke, *Applied Physics Letters* **119**, 221112 (2021).
- [128] D. O. Bracher, X. Zhang, and E. L. Hu, *Proceedings of the National Academy of Sciences* **114**, 4060 (2017).
- [129] A. L. Crook, C. P. Anderson, K. C. Miao, A. Bourassa, H. Lee, S. L. Bayliss, D. O. Bracher, X. Zhang, H. Abe, T. Ohshima, E. L. Hu, and D. D. Awschalom, *Nano Letters* **20**, 3427 (2020).
- [130] M. Mokhtarzadeh, M. Carulla, R. Kozak, and C. David, *Micro and Nano Engineering* **16**, 100155 (2022).
- [131] J. Yang, M. A. Guidry, D. M. Lukin, K. Yang, and J. Vučković, *Light: Science & Applications* **12**, 201 (2023).
- [132] D. M. Lukin, M. A. Guidry, J. Yang, M. Ghezellou, S. Deb Mishra, H. Abe, T. Ohshima, J. Ul-Hassan, and J. Vučković, *Physical Review X* **13**, 011005 (2023).
- [133] B.-S. Song, T. Asano, S. Jeon, H. Kim, C. Chen, D. D. Kang, and S. Noda, *Optica* **6**, 991 (2019).
- [134] J. Hessenauer, J. Körber, M. Ghezellou, J. Ul-Hassan, G. V. Astakhov, W. Knolle, J. Wrachtrup, and D. Hunger, *Optica Quantum* **3**, 175 (2025).
- [135] B. Merkel, A. Ulanowski, and A. Reiserer, *Physical Review X* **10**, 041025 (2020).
- [136] C. Derntl, M. Schneider, J. Schalko, A. Bittner, J. Schmiedmayer, U. Schmid, and M. Trupke, *Optics Express* **22**, 22111 (2014).
- [137] C. H. Bennett and G. Brassard, *Theoretical computer science* **560**, 7 (2014).
- [138] C. H. Bennett, G. Brassard, and N. D. Mermin, *Physical review letters* **68**, 557 (1992).
- [139] S. P. Neumann, A. Buchner, L. Bulla, M. Bohmann, and R. Ursin, *Nature Communications* **13**, 6134 (2022).
- [140] K. Azuma, S. E. Economou, D. Elkouss, P. Hilaire, L. Jiang, H.-K. Lo, and I. Tzitrin, *Reviews of Modern Physics* **95**, 045006 (2023).
- [141] R. Horodecki, P. Horodecki, M. Horodecki, and K. Horodecki, *Reviews of Modern Physics* **81**, 865 (2009).
- [142] C. H. Bennett, G. Brassard, S. Popescu, B. Schumacher, J. A. Smolin, and W. K. Wootters, *Physical review letters* **76**, 722 (1996).
- [143] F. Rozpędek, R. Yehia, K. Goodenough, M. Ruf, P. C. Humphreys, R. Hanson, S. Wehner, and D. Elkouss, *Physical Review A* **99** (2019), 10.1103/physreva.99.052330.
- [144] C. Nguyen, D. Sukachev, M. Bhaskar, B. Machiels, D. Levonian, E. Knall, P. Stroganov, R. Riedinger, H. Park, M. Lončar, *et al.*, *Physical review letters* **123**, 183602 (2019).
- [145] Without loss of generality we assume that the compensation is performed immediately after the photon measurement. In a quantum communication setting, the compensation will not be performed immediately since unitary operations on the spin are time-consuming. Instead, the measurement outcome is stored and classically communicated at a later time.
- [146] J. D. Franson, *Physical Review Letters* **62**, 2205 (1989).
- [147] P. Sohr, P. Koller, T. Astner, and M. Trupke, (2026), manuscript in preparation.
- [148] H.-K. Lo, M. Curty, and B. Qi, *Phys. Rev. Lett.* **108**, 130503 (2012).
- [149] S. Muralidharan, L. Li, J. Kim, N. Lütkenhaus, M. D. Lukin, and L. Jiang, *Scientific reports* **6**, 20463 (2016).
- [150] K. J. Wo, G. Avis, F. Rozpędek, M. F. Mor-Ruiz, G. Pieplow, T. Schröder, L. Jiang, A. S. Sørensen, and J. Borregaard, *npj Quantum Information* **9**, 123 (2023).
- [151] L. Pettersson and A. S. Sørensen, *arXiv preprint arXiv:2503.19822* (2025).
- [152] I. Devetak and A. Winter, *Proceedings of the Royal Society A: Mathematical, Physical and Engineering Sciences* **461**, 207 (2005).
- [153] S. P. Neumann, T. Scheidl, M. Selimovic, M. Pivoluska, B. Liu, M. Bohmann, and R. Ursin, *Physical Review A* **104**, 022406 (2021).

- [154] M. Hanks, M. Trupke, J. Schmiedmayer, W. J. Munro, and K. Nemoto, *New Journal of Physics* **19**, 103002 (2017).
- [155] S. Wengerowsky, S. K. Joshi, F. Steinlechner, H. Hübel, and R. Ursin, *Nature* **564**, 225 (2018).
- [156] M. N. Hall, K.-T. Foerster, S. Schmid, and R. Durairajan, *Optical Switching and Networking* **41**, 100621 (2021).
- [157] D. D. Awschalom, R. Hanson, J. Wrachtrup, and B. B. Zhou, *Nature Photonics* **12**, 516 (2018).
- [158] N. T. Son, C. P. Anderson, A. Bourassa, K. C. Miao, C. Babin, M. Widmann, M. Niethammer, J. Ul Hassan, N. Morioka, I. G. Ivanov, F. Kaiser, J. Wrachtrup, and D. D. Awschalom, *Applied Physics Letters* **116**, 190501 (2020), https://pubs.aip.org/aip/apl/article-pdf/doi/10.1063/5.0004454/14532891/190501_1_online.pdf.
- [159] N. H. Nickerson, J. F. Fitzsimons, and S. C. Benjamin, *Phys. Rev. X* **4**, 041041 (2014).
- [160] S. Pirandola, R. Laurenza, C. Ottaviani, and L. Banchi, *Nature communications* **8**, 15043 (2017).

Appendix A: Parameter list for MA-MDI-QKD simulations

Here, we list all relevant parameters used for the simulations of the MA-MDI-QKD protocol using SiC devices. The values are derived from state-of-the-art experiments and off-the-shelf component specifications. The first part of Table II lists the spin-cavity parameters, while the second part of the table lists parameters used in the simulation.

TABLE II. Parameters used in the MA-MDI-QKD simulation with SiC devices.

Name	Symbol	Value	Comment/Description
Amplitude decay time	T_1	30s	Amplitude decay time of the electron spin $\eta_r(t) = \eta_{r0}e^{-t/T_1}$.
Coherence time	T_2	10ms-10s	Dephasing time of electron spin.
Nuclear spin amplitude decay time	T_{1N}	30s	Amplitude decay time of the nuclear spin.
Nuclear spin coherence time	T_{2N}	> 10s	Dephasing time of nuclear spin.
Spin conversion time	T_{E-N}	10 μ s	Time needed for a conversion from electron spin to nuclear spin.
Spin readout time	τ_R	400 ns	Time required to measure the electron spin.
π -pulse time	τ_π	10-100 ns	π -pulse duration.
Initialization time	τ_{init}	$\tau_R + \tau_\pi$	Initialization time for the electron spin.
Reflectivity $ \uparrow\rangle$	η_\uparrow	1	Reflectivity of the cavity with the spin in the \uparrow state, SMF included.
Reflectivity $ \downarrow\rangle$	η_\downarrow	0	Reflectivity of the cavity with the spin in the \downarrow state, SMF included.
Linewidth	γ	100 MHz	Optical Fourier-limited linewidth (FWHM), including cooperative broadening.
Pulse duration	τ_p	11.2 ns	Optical pulse duration.
Writing time	τ_w	20-200 ns	$2(\tau_p + \tau_\pi)$. Time difference between the time that the beginning of the pulse arrives at the QM and the time that a successful/unsuccessful loading is declared.
Reading time	τ_r	410-500 ns	$400 \text{ ns} + \tau_\pi$. Time difference between the time that the retrieval process is applied until the end of the pulse is out.
Writing efficiency	η_w	0.13	Probability to store a qubit and herald success conditioned on having a single photon at the QMs input.
Reading efficiency	η_{r0}	1	Probability to retrieve a single photon out of the QM (right after loading $t=0$) conditioned on a successful loading in the past.
Single-photon detection efficiency	η_{SPD}	0.85	Superconducting nanowire single photon detector
Temporal resolution	t_{SPD}	50 ps	Superconducting nanowire single photon detector, FWHM
Dark count rate	γ_{dc}	100 Hz	
Background rate	γ_{bg}	0 Hz	Photonic background rate per optical mode
Channel length	L	0 – 700 km	$L_{A(B)}$ is the channel length from Alice or Bob to the respective memory. $L = L_A + L_B$, where we assume equal channel length $L_A = L_B$.
Fibre attenuation	α_{Ob}	0.3 dB/km	At the telecom O-band
Setup misalignment probability	$e_{A(B)}$	0	Probability of a qubit flip
Error correction inefficiency	f	1.16	Efficiency of the error correction code
Insertion loss fibre optical circulator	η_{oc}	0.8 dB	
Insertion loss fibre optical switch	η_{os}	0.6 dB	
Optical rise/fall time optical switch	t_{os}	8 ns	
Minimal pulse width optical switch	Δt_{os}	90 ns	